

# Doppler Tomography

T.R. Marsh

Department of Physics and Astronomy, Southampton University, Highfield,  
Southampton SO17 1BJ

**Abstract.** I review the method of Doppler tomography which translates binary-star line profiles taken at a series of orbital phases into a distribution of emission over the binary. I begin with a discussion of the basic principles behind Doppler tomography, including a comparison of the relative merits of maximum entropy regularisation versus filtered back-projection for implementing the inversion. Following this I discuss the issue of noise in Doppler images and possible methods for coping with it. Then I move on to look at the results of Doppler Tomography applied to cataclysmic variable stars. Outstanding successes to date are the discovery of two-arm spiral shocks in cataclysmic variable accretion discs and the probing of the stream/magnetospheric interaction in magnetic cataclysmic variable stars. Doppler tomography has also told us much about the stream/disc interaction in non-magnetic systems and the irradiation of the secondary star in all systems. The latter indirectly reveals such effects as shadowing by the accretion disc or stream. I discuss all of these and finish with some musings on possible future directions for the method. At the end I include a tabulation of Doppler maps published in refereed journals.

## 1 Introduction

Many rapidly rotating single and binary stars change little during the course of a single rotation or orbit. The spots on single stars can persist for many days, while cataclysmic variable stars may stay in outburst for over 100 orbits and in quiescence for ten times longer still. However, for the observer, orbital rotation can cause considerable variability both in flux and spectra. This arises from a combination of changes in aspect angle and visibility, caused by geometrical effects, and the rotation of all velocity vectors with the binary orbit. These effects are a blessing and a curse: without them we would know considerably less than we do about such stars, however the complex variability can be hard to interpret.

The method of Doppler tomography was developed to unravel the emission line variations of cataclysmic variable stars (CVs) [48]. CVs are short period binary stars, with orbital periods typically between 1.5 and 10 hours, which are beautifully set up to allow us to study accretion. The stellar components of the binary, a white dwarf and a low-mass main-sequence star, are faint, and their semi-detached configuration means that the geometry is entirely specified by the mass ratio and orbital inclination alone. Unfortunately, CVs are far too small to be resolved directly – they typically subtend  $< 10^{-4}$  seconds of arc at Earth – and we can learn nothing of their structure from direct imaging. Instead we must turn to more indirect methods. Two key methods are “eclipse mapping”,

introduced by Horne [39] and reviewed in this volume by Baptista, and “Doppler tomography”, the subject of this chapter. Eclipse mapping relies on the geometrical information contained in eclipse light curves; Doppler Tomography uses the velocity information contained in Doppler-shifted light curves.

In this paper I detail the principles behind Doppler tomography and hope to give the reader a full picture of what is now a widely-applied tool in the field. I follow the fundamentals with a short section on accounting for stochastic noise, which has usually been ignored to date, before finally moving onto a survey of results. Although I will attempt to be as self-contained as possible, the subject has become too large to cover every application of Doppler tomography and so I instead focus upon cataclysmic variable stars. I start this endeavour with a potted history of the development of Doppler tomography.

## 2 History

Although not restricted in application to CVs, since Doppler tomography was developed for CVs and has so far mostly been applied to them (with several honourable exceptions covered elsewhere in this volume), for completeness I start by describing our standard picture of CVs. Fig. 1 shows a schematic representation of our model of non-magnetic CVs with a white dwarf surrounded by a flat disc, orbiting a tidally-distorted main-sequence star. In addition a stream of matter flows from the main sequence-star and hits the disc in a spot. All of these components, as well as others, have been seen in Doppler images. In eclipsing CVs,

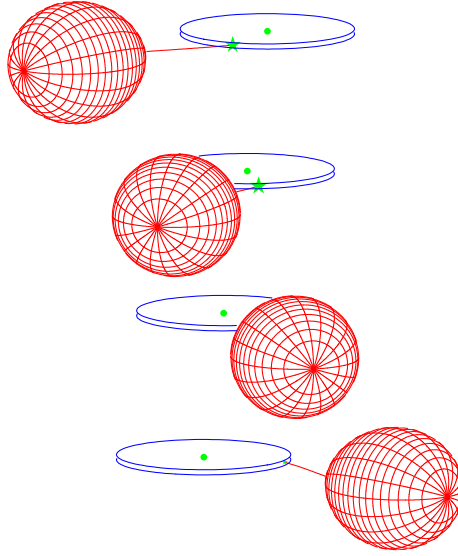


**Fig. 1.** A schematic illustration of a cataclysmic variable viewed at four orbital phases.

as seen in Fig 1, the main-sequence star occults the accreting regions allowing us to locate the chief sources of emission. It was precisely this that led to the development of the standard model in the early 1970s [89,72]. In systems with compact emission sources, the sharp ingress and egress features during eclipse allow the source location to be pin-pointed, and thus, for instance, it is possible to determine the binary mass ratio from the observed position of the gas stream impact [73,94]. What about more diffuse emission – the disc for instance? An obvious possibility is to fit a parameterised model of the disc emission to light-curves. However this is plagued by our lack of good *a priori* models. For instance, a symmetric distribution following a power-law in radius is a simple and obvious choice for modelling discs, but are discs really symmetric and what if they do not follow power-laws? These problems were solved by Keith Horne who during his thesis work introduced the powerful idea of regularised fitting to the study of CVs [39]. Horne modelled the accretion regions with a grid of many independent pixels, effectively giving a model of great flexibility. To escape the degeneracy engendered by such an approach, Horne selected the image of “maximum entropy” where the entropy  $S$  is given (in the simplest case) by

$$S = - \sum_{i=1}^M p_i \ln p_i. \quad (1)$$

Here  $p_i$  is given by

$$p_i = \frac{I_i}{\sum_{j=1}^M I_j}, \quad (2)$$

where  $I_i$  is the image value assigned to pixel  $i$ . This is the method of eclipse mapping.

In eclipse mapping a one-dimensional light curve leads to two-dimensional map. Emission lines on the other hand, as I will explain, contain the extra dimension of velocity and so can give better constrained images (albeit with some disadvantages). Horne realised that the formation of the line profile from a disc was analogous to the formation of medical X-rays used in computed tomography to image the human brain. This led to the development of Doppler tomography [48], implemented in the first instance in a way analogous to eclipse mapping, using maximum entropy regularisation.

Since that time, and following articles focussing upon the more accessible filtered back-projection inversion [40,62], the use of Doppler tomography has exploded, with over 100 refereed publications making use of it or containing theoretical simulations of Doppler images (Fig. 2). Doppler maps have been published for some 16 dwarf novae, 13 AM Her stars, 11 DQ Her stars, 16 nova-like variables and 5 black-hole systems, along with other types such as Algols and Super-Soft sources. Doppler tomography is approaching the status of a standard tool; I now begin discussion of its underlying principles.

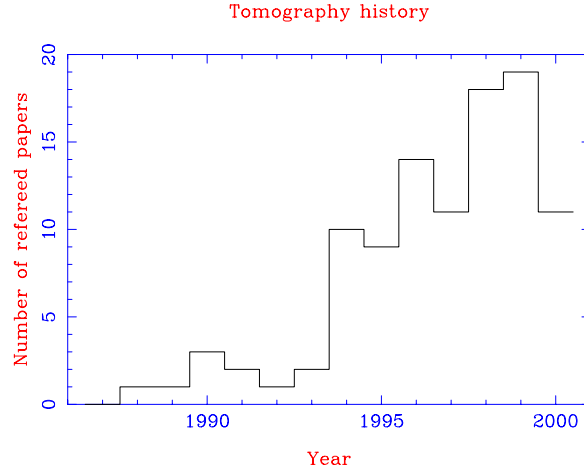


**Fig. 2.** Numbers of refereed publications using Doppler tomography versus year of publication.

### 3 The principles of Doppler tomography

Doppler tomography arose from a desire to interpret the emission-line profile variations of accretion discs. Past papers on tomography have started by describing the formation of the double-peaked profiles from discs [48]. However, the existence of a disc is not necessary for Doppler tomography. For instance, one of the most spectacular applications of tomography has been to the AM Her stars or polars [67], systems in which the white dwarf has such a strong magnetic field that there is no disc. Therefore, in this instance, I will attempt to describe tomography from a more general perspective.

The key to tomography is first to consider a point-like source of emission in a binary. Assuming this has a motion parallel to the orbital plane of the binary, line emission from such a source will trace out a sinusoid around the mean velocity of the system. Assuming one observed such a sinusoid, one could associate it with a particular velocity vector in the binary, depending upon its phase and amplitude. The trick of tomography is to cope with any number of such sinusoids, even when they are so overlapped and blended that one cannot distinguish one from another. To understand how this is possible, it is helpful to think of profile formation as a projection in the mathematical sense of integrating over one dimension of an  $N$ -dimensional space to produce an  $N - 1$  dimensional space.

#### 3.1 Profile formation by projection

A given point in the binary can be defined by its spatial position, but, more usefully in this case, also by its velocity  $(V_x, V_y)$ . One must be a little careful to define this velocity which is relative to the *inertial* rather than rotating frame.

Inertial frame velocities are always changing as the binary rotates, and so in order to define unique values of  $V_x$  and  $V_y$ , they are measured at a particular orbital phase. Conventionally this is taken to be when the inertial frame lines up with the rotating frame. In the case of CVs it is usual to define the  $x$ -axis (in the rotating frame) to point from the white dwarf to the mass donor, and the  $y$ -axis to point in the direction of motion of the mass donor. With this convention, and defining orbital phase zero to be the moment when the donor star is closest to us, the radial velocity of the point in question at orbital phase  $\phi$  is

$$V_R = \gamma - V_x \cos 2\pi\phi + V_y \sin 2\pi\phi, \quad (3)$$

where  $\gamma$  is the mean or systemic velocity of the star. The use of a single value of  $\gamma$  is equivalent to assuming that all motion is parallel to the orbital plane as mentioned above.

With these definitions, an “image” of the system can be defined as the strength of emission as a function of velocity,  $I(V_x, V_y)$ . That is, the flux observed from the system that comes from the velocity element bounded by  $V_x$  to  $V_x + dV_x$ ,  $V_y$  to  $V_y + dV_y$  is given by  $I(V_x, V_y) dV_x dV_y$ . I will refer to this as an “image in velocity space” or more simply a “velocity-space image”. The relation of this image to the conventional image will be discussed below.

The line flux observed from the system between radial velocities  $V$  and  $V + dV$  at orbital phase  $\phi$  can now be obtained by integration over all regions of the image that have the correct radial velocity:

$$\int_{-\infty}^{\infty} \int_{-\infty}^{\infty} I(V_x, V_y) [g(V - V_R) dV] dV_x dV_y, \quad (4)$$

where  $g$  is a function (of velocity) representing the line profile from any point in the image, including instrumental blurring. I assume here that  $g$  is the same at every point, although it is possible to allow it to vary. The velocity width is divided out to obtain a flux density of course, and so the line profile can be expressed as

$$f(V, \phi) = \int_{-\infty}^{\infty} \int_{-\infty}^{\infty} I(V_x, V_y) g(V - V_R) dV_x dV_y. \quad (5)$$

Ideally  $g$  is narrow, best of all a delta function, thus this equation picks out all regions of the image close to the line

$$V = V_R = \gamma - V_x \cos 2\pi\phi + V_y \sin 2\pi\phi.$$

This is a straight line in  $V_x, V_y$  coordinates. Different values of  $V$  define a whole family of parallel straight lines across the image, with a direction dependent upon the orbital phase. With the definition of velocity and orbital phase described above, orbital phase 0 corresponds to a collapse in the positive  $V_y$  direction, phase 0.25 corresponds to the positive  $V_x$  direction, phase 0.5 to the negative  $V_y$  direction etc, with the angle rotating clockwise. Thus the formation of the line profile at a particular phase can be thought of as a projection (or collapse) of

the image along a direction defined by the orbital phase. Note that if this model is correct, two line profiles taken half-an-orbit apart should be mirror images of one another. The extent to which this is not the case is one measure of violations of the basic assumptions made.

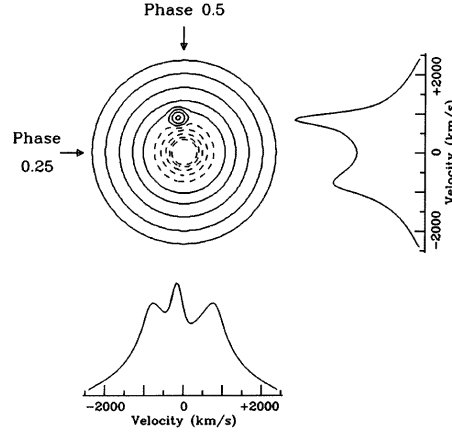


**Fig. 3.** A model image and the equivalent profiles formed by projection at angle appropriate to orbital phases 0.25 (right-most profile) and 0.5 (lower profile).

Fig. 3 shows a pictorial representation of this process for two projection angles. The artificial image has been created with a spot which can be seen to project into different parts of the profile at different phases. Tracing back from the peaks along the projection directions leads to the position of the original spot. This is in essence how line profile information can be used to reconstruct an image of the system.

A series of line profiles at different orbital phases is therefore nothing more than a set of projections of the image at different angles. The inversion of projections to reconstruct the image is known as “tomography”, the case of medical X-ray imaging being perhaps the most famous, although it occurs in many other fields too. I now look at the two methods that have been applied in the case of Doppler tomography.

### 3.2 Inversion Methods

The mathematics of the inversion of projections dates back to the work of Radon in 1917 [60]. If one knows the function (in my notation)  $f(V, \phi)$  for all  $V$  and  $\phi$ , a linear transformation – the Radon transform – can produce the desired end product,  $I(V_x, V_y)$ . In reality, things are not so easy, and we never have the luxury of knowing the line profiles at all orbital phases, although one can get close in some cases. With the advent of fast computers and the development of medical imaging, interest in the implementation of Radon’s transform

increased greatly in the 1970s, and one particular method, that of “filtered back-projection” found favour [63]. The original paper on Doppler tomography used an alternative method inherited from eclipse mapping, that of maximum entropy regularisation. In this section I describe these two methods, which are both in use today. Each has its pros and cons, which I discuss at the end of the section.

**Filtered back-projection** The mathematical inversion of Eq. 5 is detailed in the Appendix A. The process can be summarized in the following two steps. First the line profiles are filtered in velocity to derive modified profiles,  $\tilde{f}(V, \phi)$ . The filter is applied through a Fourier transform, multiplication by  $|s|/G(s)$ , where  $G(s)$  is the Fourier transform over  $V$  of  $g(V)$  and  $s$  is the frequency in inverse velocity units, and finally an inverse Fourier transform. It can be applied to one spectrum at a time and is a fairly fast process.

The second step is that of *back-projection*:

$$I(V_x, V_y) = \int_0^{0.5} \tilde{f}(\gamma - V_x \cos 2\pi\phi + V_y \sin 2\pi\phi, \phi) d\phi. \quad (6)$$

An intuitive understanding of back-projection is extremely useful when trying to make sense of Doppler maps. There are two ways of imagining the process (see Fig. 4). The first one is perhaps the most obvious from Eq. 6 which implies

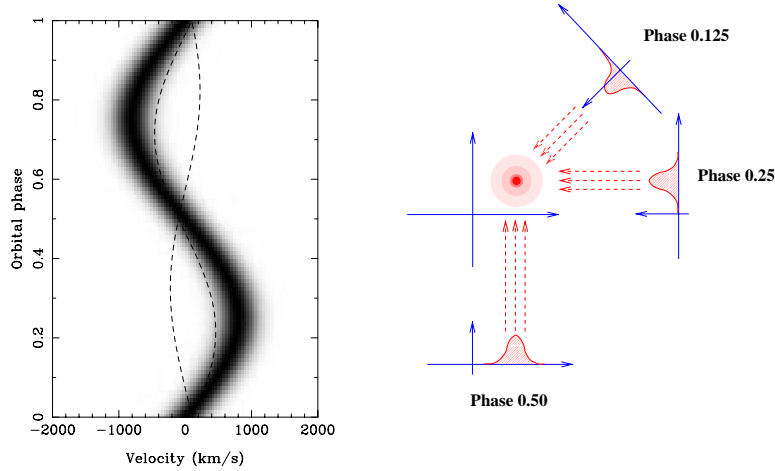


**Fig. 4.** Two view of back-projection: on the left are paths of integration through trailed spectra (spectra plotted as greyscale images with time running upwards and wavelength from left to right). A track close to a sinusoidal component gives a spot in the final image. On the right three profiles are smeared back along their original projection directions to give a spot.

that each point in the image can be built by integration along a sinusoidal path

through “trailed” spectra (spectra viewed in 2D form with axes of phase versus velocity). The particular sinusoid is exactly that which a spot at the particular place in the image would produce in the trailed spectrum. This view is illustrated on the left of Fig. 4.

However, back-projection is named for another, perhaps more useful, way of regarding this operation shown on the right of Fig. 4. In effect, Eq. 6 means that the image is built up by smearing each filtered profile along the same direction as the original projection which formed it. This way of looking at back-projection shows very clearly why small numbers of spectra cause linear artifacts in Doppler maps, and one should always be wary of such features. Similarly, any anomalies, such as unmasked cosmic rays, dead pixels, flares or unmasked eclipses are liable to cause streaks across Doppler maps.

If the local line profile  $g(V)$  is gaussian then so too is  $G(s)$ , dropping to zero at large  $s$ . Thus the filter  $|s|/G(s)$  will strongly amplify high frequencies, and the image will be corrupted by noise. This may be familiar when it is realised that division by  $G(s)$  is just the standard (and noise-sensitive) Fourier deconvolution; the presence of  $|s|$  in this case only exacerbates the problem. One can just remove the  $G(s)$  term and thus make no attempt to de-convolve the image. Typically one goes further still and the filter applied is  $|s|W(s)$ , where  $W(s)$  is a (typically gaussian) “window” function to cut off high frequencies and therefore limit the propagation of noise into the final image. The penalty for this is that the final image is a blurred version of the true image. A similar trade-off will become apparent in the maximum entropy inversion which I turn to now.

**Maximum Entropy Inversion** In the original paper presenting Doppler tomography, the focus was upon an alternative to filtered back-projection using maximum entropy regularisation [48]. This stemmed in part from the earlier development of eclipse mapping but also because I originally developed Doppler tomography in spatial coordinates in which the projection becomes one over a set of curves rather than straight lines [47]. However, velocity space is nearly universally used now, and the linear inversion has become more commonly used on the whole. Is another inversion method useful? I think the answer is yes, and will discuss why in detail below. First of all, I describe the maximum entropy method in some more detail.

The application of maximum entropy to Doppler tomography is very similar to the eclipse mapping case: a grid of pixels spanning velocity space is adjusted to achieve a target goodness-of-fit, measured by  $\chi^2$ . In general there are an infinite number of such images and so the image of maximum entropy is selected. A refined form of entropy which measures departures from a “default” image [39] is used:

$$S = - \sum_{i=1}^M p_i \ln \frac{p_i}{q_i}. \quad (7)$$



Here all symbols are as before with the addition of

$$q_i = \frac{D_i}{\sum_{j=1}^M D_j}, \quad (8)$$

where  $\mathbf{D}$  is the default image. The default image is important in eclipse mapping (see Baptista, this volume) but less so in Doppler tomography. Usually a moving default is used, computed as a blurred version of the image. This constrains the map to be smooth on scales shorter than the blurring, but fixed by the data alone on larger scales. For reasonable data, the choice of default appears to have little effect. Indeed, it would be my guess that neither does the form of  $S$ , and that its most important role in this case is to allow a unique solution to be found.

**Relative merits of the two inversions** Table 1 compares the Maximum Entropy Method (MEM) and Filtered Back-Projection (FBP) inversion methods; plus and minus signs indicate pros and cons respectively. First of all,  $\chi^2$  in the

Characteristic	MEM	FBP
Controlling parameter	$\chi^2$	FWHM of noise filter
Processor time	– (22 sec) <sup>†</sup>	+ (0.7 sec)
Comparison with data	++	--
Consistency of noise level	– <sup>‡</sup>	+
Flexibility	++	--

<sup>†</sup>100 by 100 image, 100 by 50 data, 300 MHz Pentium II.

**Table 1.** Comparison of maximum entropy and filtered back-projection for Doppler tomography.

maximum entropy method (MEM) is identified as the equivalent of the window filter in the filtered back-projection (FBP). For instance a low  $\chi^2$  forces the image to become highly structured in order to fit the data better. Conversely, a high  $\chi^2$  allows the image to become smooth and blurred. Next I compare processing time, which is perhaps the major disadvantage of MEM. In the example given, MEM took 30 times longer than FBP. Even so, for single images the absolute amount of time taken is not large, especially when compared with the steps taken to get the data in the first place, although it can become more significant when trying to estimate noise, as I will discuss later. Nevertheless, I still regard it as a relatively minor disadvantage, and award a single minus. The next entry “Comparison with data” refers to the central role that  $\chi^2$  plays in the MEM reconstructions which allows one to compare the predicted data directly to observations. Filtered back-projection does not try to achieve a good fit to the data, leaving one uncertain as to how much better the fit could have been; I regard this as a significant disadvantage of the method.

Propagation of noise into MEM images can be problematical when one is comparing, say multiple datasets. The reason is that if one sets the same  $\chi^2$

level for each inversion, in one case this might be easy to reach and a rather smooth looking map is the result, while in the next may have a hard time reaching the desired level at all, resulting in a noisy map. FBP on the other hand seems to give an images of similar appearance for the same window filter. It was for this reason that Marsh & Duck [52] used FBP in their tomography of the DQ Her star, FO Aqr. It is possible that this problem could be fixed by iterating towards a fixed entropy and minimising  $\chi^2$ . While this may seem a bit *ad hoc*, it may provide a more accurate representation of how one actually sets  $\chi^2$  in practice: it is rather rare to achieve statistically acceptable values of  $\chi^2$  for data of reasonably good signal-to-noise ratio, and often  $\chi^2$  is set so that the image is neither too smooth nor too corrupted by noise.

Flexibility, the final entry in Table 1, is another major plus point of MEM. For instance, it is very easy to adapt it to the common case of blended lines [48,53]. Steeghs (this volume) presents a nice extension of MEM to allow for variation of flux with orbital phase. Another more minor example of this is that it is easy in MEM to mask out bad data without the need to interpolate.

For straightforward cases, I think that there is relatively little to choose between the two methods, although the speed of the filtered back-projection may be advantageous when many maps are being computed. MEM has the edge in difficult cases where modifications of the standard model are needed.

### 3.3 Noise in Doppler images

In the penultimate part of this section, I look at the propagation of noise into Doppler maps. To an extent Doppler images carry their own uncertainty estimates in the degree of fluctuation that one sees in the background, and perhaps this has motivated the lack of a more rigorous treatment to date. Moreover, it is often the case, as I remarked above, that Doppler tomography cannot achieve a good fit to the data, and one must assume that systematic errors are dominant. However, there is still a need to understand noise, with a common case being the question of the reality of a certain feature. Appealing to the level of background noise is not always good enough – for example, any map will have a highest point, but how is one to judge whether it is significant?

It has been said that noise cannot be propagated into Doppler maps [84]. It is in fact straightforward to do so. However, the important point to understand is that noise in Doppler images is *correlated*. In more detail it is correlated on short scales but less so on large scales. This correlation means for example that single pixel variances are more-or-less useless in defining the amount of noise on a Doppler image. The correlation is positive on short scales and so Doppler maps are effectively noisier than an uncorrelated image with the same variance per pixel; the difference is significant.

One of the best ways to appreciate the correlation is to view animations running simulated images in movie form. Since this is not possible in print, I illustrate the consequence by plotting the scatter in circular apertures in Fig. 5. In this figure, although the RMS scatter of the uncorrelated images was adjusted to match the MEM images pixel-by-pixel, the scatter at first grows more quickly

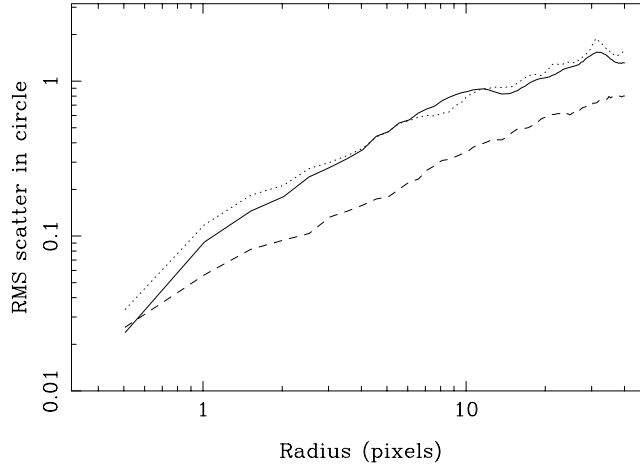


**Fig. 5.** The figure shows the RMS scatter in simulated Doppler images measured in circular apertures, as a function of the aperture radius for three sets of simulations. The solid line shows results of MEM inversions with  $\chi^2 = 1.0$ ; the dotted line shows the FBP results with a filter of FWHM = 1.0 in terms of the Nyquist frequency; the dashed line shows what the result would have been if the noise were uncorrelated with the same variance per pixel as the MEM simulations.

with radius in the FBP and MEM images, leading to an RMS about 3 times larger at large radii. This illustrates the positive correlation at small separations. Ignoring this correlation would lead to a very significant underestimate of the true noise. In this case for radii larger than  $\approx 4$  pixels, all three lines are roughly parallel, demonstrating the weak correlation on large scales. The final point is the very similar behaviour of the FBP and MEM plots: the two methods lead to a very similar propagation of noise into the image.

The exact pattern of noise is dependent upon the controlling parameter,  $\chi^2$  or the filter FWHM. While driving down  $\chi^2$  may force a better fit and higher resolution, a penalty is paid in increased noise. Fig. 6 shows this effect. In this case as  $\chi^2$  is lowered from 1.1 to 0.9, the noise at the smallest scales increases by a factor of two; large scales are almost unaffected. Very similar behaviour is seen for different filter widths for filtered back-projection.

Figures 5 and 6 were made by adding noise to a simulated dataset and then reconstructing images. A similar method was employed by Hessman & Hopp in their analysis of GD 552 [35]. In practice, the “bootstrap” method [15] is preferable. In this technique, real data are used to generate artificial data by randomly selecting, *with replacement*,  $N$  new points from  $N$  old points. The beauty of this method is that it automatically accounts for the true statistics of the data and one is not adding extra noise. Consider then an image with a feature one wants to characterise. As long as an explicit measurement of the feature can be devised, then multiple bootstrap runs can be used to generate an uncertainty as well.

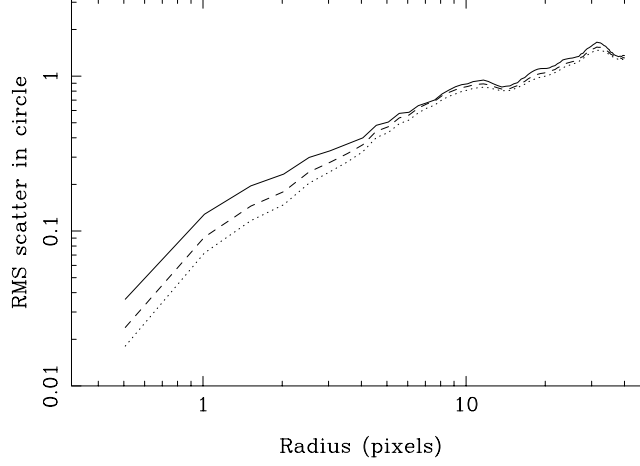


**Fig. 6.** The figure shows the RMS scatter in MEM simulations measured in circular apertures for  $\chi^2 = 0.9$  (solid line), 1.0 (dashed), and 1.1 (dotted).

As an example of how one might use the bootstrap method, consider an image showing evidence for a bright-spot, with some question as to the significance of the feature (Fig. 7). First one needs a method of measuring the strength of such a feature. The method I use here is first to subtract off the symmetric part of the image and then to measure the flux in a circular aperture centred on the spot. I then use the following procedure to determine the significance of the feature:

1. Generate a large number ( $\sim 1000$ ) of new datasets from the original data by bootstrap resampling (a fast procedure).
2. Compute maps for each of these in the same manner as for the true map (here the CPU penalty of MEM is paid in full).
3. Subtract the true map from each boot-strapped map to obtain difference maps.
4. Measure the flux of each difference map in the same way as before i.e. by subtracting the symmetric part of each image and computing the flux in a circular aperture.
5. Finally, rank the observed flux relative to the fluxes measured from the difference maps.

This procedure generates a set of values showing the stochastic noise level in the circular aperture. If carried out for apertures centred on every pixel in the image, one can generate a “significance map” which shows the fraction of fluctuation values that the observed value exceeds. The result of such a scheme is shown in Fig. 7 where an artificial image shown in the top-left led, after the addition of gaussian noise, to the trailed spectrum shown in the top-right. The “true map” referred to above is displayed in the lower-left and shows evidence for a spot in the upper-left quadrant. Carrying out the bootstrap computations with

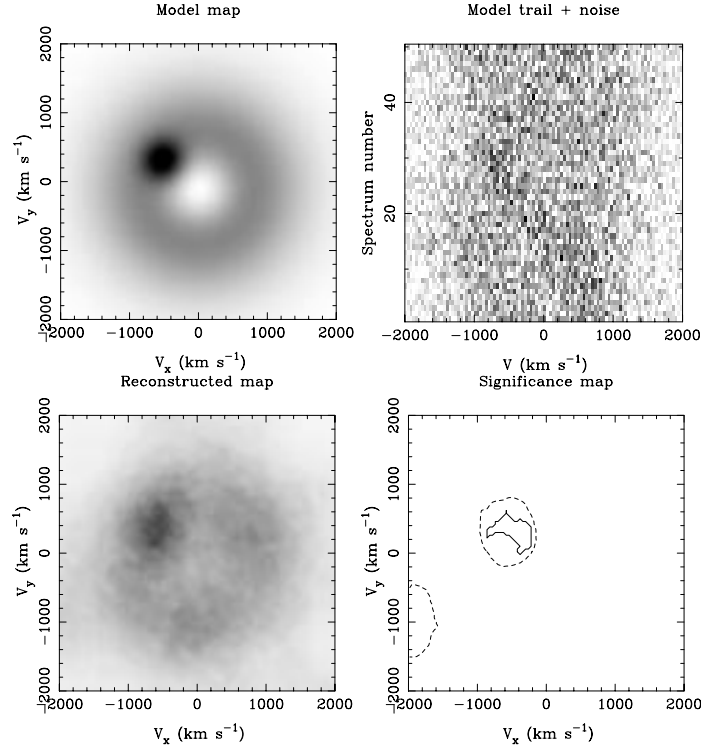


**Fig. 7.** The panels show an initial test map (upper-left), the equivalent trailed spectrum with noise added (upper-right), the reconstructed image (lower-left) and finally the lower-right panel shows contours encircling regions of the reconstruction above 99% of the 1000 trials (dashed) and 100% of them (solid).

1000 trials leads to the significance map of the lower-right. This shows that the region of the spot is higher than all 1000 of the simulated datasets, whereas no other part of the image is. In this case the circular aperture used has a radius of  $200 \text{ km s}^{-1}$ , and so can be fitted  $\sim 100$  times over into the image. Taking these to be independent, then there is  $\sim 10\%$  chance that one region will exceed all 1000 trials. More trials would be needed to establish the reality of the feature more firmly, but the principle is clear.

Similar measurements are easily imagined, for instance, one could perhaps fit the position of the spot [35], and subsequently obtain uncertainty estimates from bootstrapping. All that is necessary is that the measurement is precisely defined and applied in the same way to the true and bootstrap maps.

### 3.4 Axioms of Doppler Tomography

Doppler tomography rests on certain approximations to reality that are, at best, only partially fulfilled. Violation of these approximations does not mean that the

resulting maps are useless, but everyone who carries out Doppler tomography should be aware of its limitations. Thus in this final part of this section, I list the “axioms” that underly the method:

1. All points are equally visible at all times.
2. The flux from any point fixed in the rotating frame is constant.
3. All motion is parallel to the orbital plane.
4. All velocity vectors rotate with the binary star.
5. The intrinsic width of the profile from any point is negligible.

Exceptions exist to each of these. For instance, emission on the mass donor violates the first axiom, while outbursts clearly contravene (2). Doppler tomography is an interpretation of the data within a specific model of binary systems and only applies inasmuch as the model itself does.

## 4 The application of Doppler tomography to CVs

I now move on to discuss Doppler tomography in the context of cataclysmic variable stars. I will mainly focus upon results, but before doing so I consider the interpretation of Doppler maps in the case of CVs.

### 4.1 Understanding Doppler maps

On the basis of the standard model presented in section 2 one can easily predict the locations of the various components in velocity-space; Fig. 8 shows some of the key components of a CV represented in velocity space. The donor star

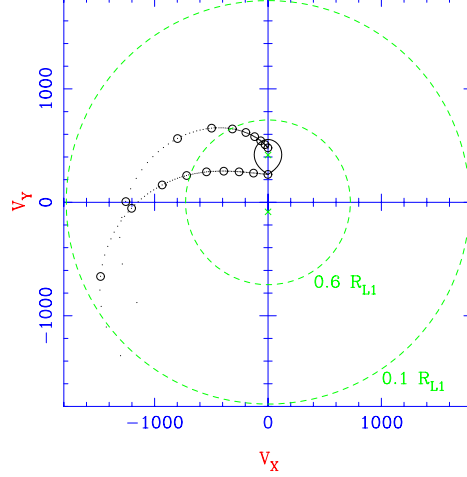


**Fig. 8.** A schematic of some key components in velocity coordinates.

is assumed to co-rotate with the binary, which means that it appears with the same shape in velocity as it does in position coordinates, although rotated by  $90^\circ$  owing to the relation  $\mathbf{v} = \boldsymbol{\Omega} \wedge \mathbf{r}$  between velocity and position for “solid-body” rotation. This reassuring property is somewhat misleading, since the disc, which is very definitely not co-rotating with the binary, ends up being turned inside out so that the inner disc is at large velocities while the outer disc appears as a ring at low velocity. The gas stream is plotted twice: once with its true velocity and once with the velocity of the disc along its path; one can also imagine intermediate cases. The positions of all these components is fully specified if the projected orbital velocities of the two stars,  $K_1$  and  $K_2$ , and the orbital phase are known. The overall scale is set by  $K_1 + K_2$ ; their ratio, which is the mass ratio  $q = K_1/K_2 = M_2/M_1$ , defines the detailed shape of the stream and Roche lobe. The orbital phase sets the orientation of the image, and if it is not known the image will be rotated by an unknown amount relative to the “standard” orientation shown in Fig. 8. This is not uncommon: for instance if the orbital phase is based upon emission line measurements, it is typically delayed by 0.05 – 0.1 cycles with respect to the true ephemeris. This causes an anti-clockwise rotation of the image by an equivalent number of turns. The published map of LY Hya [78] is a nice example of this phenomenon.

Although velocity coordinates simplify the picture of line profile formation, it is simple enough to invert into position coordinates – indeed this is how I originally computed Doppler images [47]. All that is required is a specification of the velocity at every point in the system. However, I abandoned this approach for two reasons. First, the translation between velocity and position is often not known. In fact, perhaps it is never known, given that it is likely that deviations from keplerian flow occur. This means that position maps would require recomputation each time system parameters were updated. Second, the same place in the system can produce emission at more than one velocity. This is not an abstract possibility, but happens in almost every system that has been imaged. There are many examples of bright-spot emission from the gas stream while the disc at the same location produces emission at a completely different velocity. If such data is imaged into position coordinates on the basis of keplerian rotation, a spot of emission would be produced at a spurious location in the disc. Sticking to velocity coordinates is a reminder of these potential difficulties of interpretation. Only in eclipsing systems is there potential for disentangling such effects.

While we cannot translate the data into position space, there is no difficulty in translating any theoretical model into velocity coordinates. Indeed, ideally, the theory–data comparison should be made by predicting trailed spectra, doing away with the need for Doppler maps altogether. However, Doppler maps still have a rôle in that theoretical models are not good enough to predict all the peculiarities of real systems, and comparison is easier in the half-way house of velocity space.

The idea of translating to velocity space also applies to how one should think about Doppler maps. Rather than trying to translate features of maps mentally from velocity to position coordinates, one should try to think of various com-

ponents and imagine where they would appear in velocity space. The difference may seem slight, but it is a significant one. With that said, I now turn to look at some results.

## 4.2 Doppler imaging results

There are now a large number of examples of Doppler tomography, covering CVs along with other types of binary as well, such as Algols and X-ray transients, the latter being very similar to CVs in many ways [51,8]. Rather than spend space covering these in detail when the original references do so already, as do other contributions in this volume, I have decided to devote this section mainly to highlights based upon a literature survey of as many published Doppler images as I could find. The results of this survey are tabulated in Tables 2, 3 and 4 contained in Appendix B where I list systems with published maps, which lines were mapped, the spectral resolution, the outburst state and some indication of the appearance of the maps.

**Spiral shocks** The discovery by Steeghs et al. [77] of spiral shocks in the dwarf nova IP Peg is perhaps the most significant result from Doppler tomography applied to CVs. These shocks appear to be present in all outbursts of IP Peg,

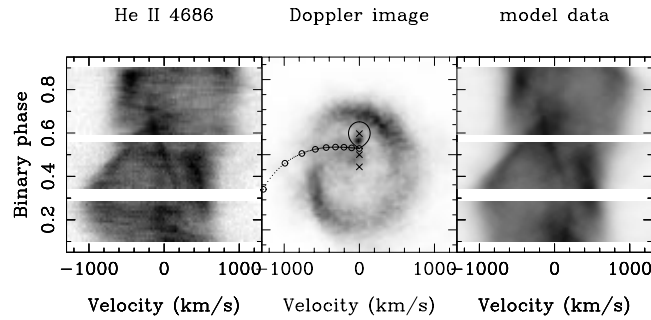


**Fig. 9.** Spiral shocks in IP Peg [27].

including (with hindsight!) pre-discovery outburst data [50]; Fig. 9 shows one example. There is corroborating evidence from other systems such as SS Cyg [76], V347 Pup [82] and EX Dra [42], although none of these are as convincing as IP Peg.

**Stream emission in polars** Beautiful work by Schwöpe and others [66,67,30,68,71] has revealed the gas stream in the polar class of cataclysmic variables in which the white dwarf is magnetically locked to the mass donor star. Although initially ballistic, there is evidence for the influence of the field upon the stream and some



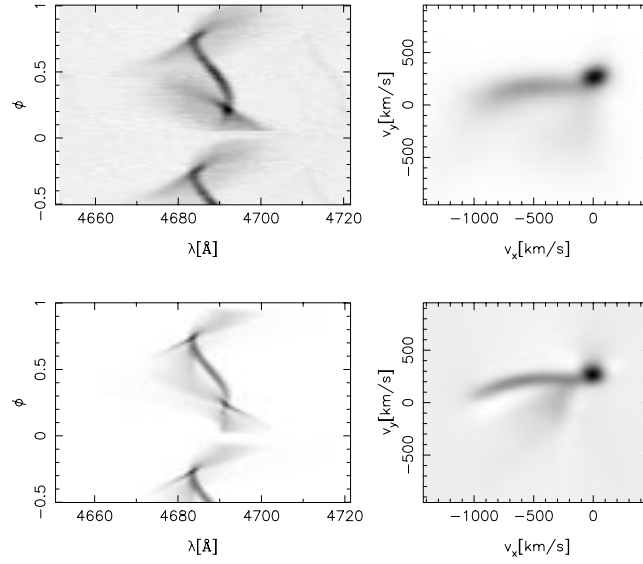


**Fig. 10.** Stream-stripping in HU Aqr [30]. The upper panels show the HeII 4686 line and Doppler map; the lower panels show simulated data based upon a simple model in which gas is pulled of the stream and threaded onto the magnetic field.

emission from the gas as it hurtles down towards the white dwarf (see Fig. 10). Such work has tremendous scope for teaching us about the stream/magnetosphere interaction. Changes in the appearance of maps between high and low states have been seen in HU Aqr [67] and further observation of differing states should tell us how the plasma/field interaction varies with accretion rate.

**Bright-spots** Many systems show bright-spots in Doppler maps, classic cases being WZ Sge [75] and GP Com [53]. The locations of the spots are interesting. In some cases they line up with the stream’s velocity [50], while others are closer to the disc’s velocity [93]. Still others adopt a position half-way between the disc and stream velocities [49,75] (see also Fig 11). There is some evidence for extended cooling following the spot [75] and there is potential for examining this with lines of differing excitation.

**Emission from the secondary star** Many Doppler maps show emission from the secondary star [50,49,23,57,66]. Some of this may be related to magnetic activity of these rapidly rotating stars, but there is little doubt that much of it is caused by irradiation by the inner disc. The disc systems are interesting in this respect since one can expect the disc to cast a shadow over the equator of the mass donor. This seems indeed to be the case [28,57] and perhaps has the potential to tell us about the vertical structure of the disc.

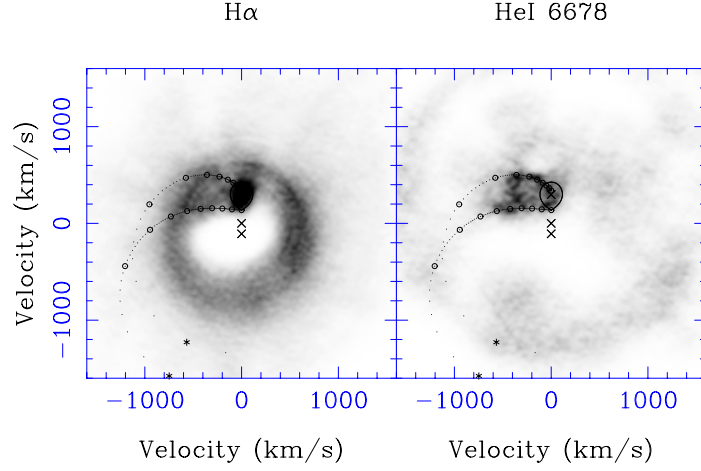


**Fig. 11.** The peculiar bright-spot of U Gem observed in January 2000 (Unda et al in prep).

**Missing discs in novalikes** Nova-like variable stars are thought to be classic examples of steady-state systems. Spectroscopically however they have proved hard to understand. A particular peculiarity of these stars is that it is often difficult to see any sign of a disc in these systems. Instead the Doppler maps are often dominated by a single structure-less blob. This blob tends to be located in the lower-left quadrant of the map for the Balmer and HeI lines, but rather closer to the expected location of the white dwarf for HeII. Several explanations for these phenomena have been proposed but none of them are compelling in my view.

## 5 The future of Doppler tomography

The future development of Doppler tomography splits into extensions of the method and the acquisition of further datasets. Dealing first of all with the latter, it is evident from Tables 2, 3 and 4 that there are several areas where improvements are possible. For instance more lines could be covered, especially metal lines (e.g. CaII), ultraviolet and infra-red lines. H $\alpha$  has received relatively little attention, but when it has been looked at, often appears peculiar [81,76]. In the case of dwarf novae, the discovery of spiral shocks makes extended coverage of outbursts of considerable interest.

Multi-epoch tomography is probably the most gaping hole because it is hard to make a coherent picture of the many one-off maps that have been published to date. The resolution of maps published to date is poor or moderate in many cases, limiting their usefulness. The ultimate limit is set by thermal broadening, but we are very far off this in most cases, especially for heavy elements. Pushing to high resolution is not trivial because of the concomitant need to shorten the

exposure time owing to smearing, but it is thoroughly feasible. Exposures of length  $t$  can be thought of as blurring the image by a rotation of

$$360^\circ \frac{t}{P}$$

where  $P$  is the orbital period. For a feature a speed  $K$  from the centre of mass, this will match the spectral resolution  $\Delta V$  when

$$\frac{t}{P} \sim \frac{1}{2\pi} \frac{\Delta V}{K}.$$

Thus if  $\Delta V$  is lowered by a factor of two, the exposure time must also be reduced by a factor two. As a concrete example, consider trying to image the mass donor in a system where  $K_2 = 400 \text{ km s}^{-1}$ . Typical equatorial velocities in CVs are  $\approx 100 \text{ km s}^{-1}$ , so we may attempt to obtain data with  $\Delta V = 10 \text{ km s}^{-1}$ . We would then need  $\Delta\phi = t/P < 0.004$ , equivalent to  $t < 30 \text{ s}$  for a system of  $P = 2$  hours. For many CVs, this will require 8m-class telescopes.

Various extensions are possible, and have already been developed in some cases. Standard Doppler tomography does not treat the geometry of the donor star correctly. It is straightforward to fix this [64]. Bobinger et al. [3] describe a method for simultaneous Doppler and eclipse mapping of emission lines in which a single image is computed to fit both spectra and light curves of the lines, with a keplerian velocity field used to translate between position and velocity space. It is difficult to evaluate whether the spectra or fluxes dominate the final maps, but it is clear that spectral information does alleviate the degenerate nature of eclipse mapping. Of course, the need to assume a particular velocity field is a disadvantage. An attempt has been made to avoid this by simultaneously adjusting a spatial image and a position-velocity map to fit spectra of eclipsing systems [1]. In this method, spectra out of eclipse serve to fix the velocity space image as usual, which is then translated to position space through the eclipse information. The technique was able to recover a  $V \propto R^{-1/2}$  relation from spectra of V2051 Oph, but as developed it could not handle the difficult case of the same place producing emission at more than one velocity. Finally Steeghs (this volume) describes a new modification which allows orbital variability to be included in Doppler images. As this is so common, it has considerable potential.

## 6 Conclusions

I have reviewed the principles and practice of the analysis method of Doppler tomography which helps the interpretation of the complex line profile variations from close binary stars. The key discoveries from the application of this technique are the spiral shocks in outbursting dwarf novae and the stream/magnetic field interaction in the polar class of cataclysmic variable stars, but Doppler tomography has taught us much about the stream/disk interaction and irradiation of the donor star too.

For the future, efforts need to be made to acquire multi-epoch datasets for tomography as these are wholly lacking at present. Following that higher spectral and temporal resolution data are needed to exploit tomography to its limit.

## References

1. Billington, I., 1995, PhD Thesis, Oxford University.
2. Billington, I., Marsh, T.R., Dhillon, V.S., 1996, MNRAS, 278, 673–682.
3. Bobinger, A. et al., 1999, A&A, 348, 145–153.
4. Burwitz, V. et al., 1998, A&A, 331, 262–270.
5. Casares, J. et al., 1995, MNRAS, 274, 565–571.
6. Casares, J., Charles, P.A., Marsh, T.R., 1995, MNRAS, 277, L45–L50.
7. Casares, J. et al., 1996, MNRAS, 278, 219–235.
8. Casares, J. et al., 1997, New Astronomy, 1, 299–310.
9. Casares, J. et al., 1997, New Astronomy, 1, 299–310.
10. Catalán, M. S., Schwöpe, A. D., Smith, R. C., 1999, MNRAS, 310, 123–145.
11. Dhillon, V.S., Marsh, T.R., Jones, D.H.P., 1991, MNRAS, 252, 342–356.
12. Dhillon, V.S., Jones, D.H.P., Marsh, T.R., Smith, R.C., 1992, MNRAS, 258, 225–240.
13. Dhillon, V.S., Jones, D.H.P., Marsh, T.R., 1994, MNRAS, 266, 859.
14. Dhillon, V.S., Marsh, T.R., Jones, D.H.P., 1997, MNRAS, 291, 694.
15. Diaconis, P., Efron, B., 1983, Sci. Am. 248, 96–.
16. Diaz, M. P., Steiner, J. E., 1994, ApJ, 425, 252–263.
17. Diaz, M. P., Steiner, J. E., 1994, A&A, 283, 508–514.
18. Diaz, M. P., Steiner, J. E., 1995, AJ, 110, 1816.
19. Diaz, M. P., Hubeny, I., 1999, ApJ, 523, 786–796.
20. Dickinson, R. J. et al., 1997, MNRAS, 286, 447–462.
21. Gaensicke, B. T. et al., 1998, A&A, 338, 933–946.
22. Harlaftis, E.T., Marsh, T.R., Dhillon, V.S., Charles, P.A., 1994, MNRAS, 267, 473.
23. Harlaftis, E.T., Marsh, T.R., 1996, A&A, 308, 97–106.
24. Harlaftis, E. T., Horne, K., Filippenko, A. V., 1996, PASP, 108, 762.
25. Harlaftis, E. T., Steeghs, D., Horne, K., Filippenko, A. V., 1997, AJ, 114, 1170–1175.
26. Harlaftis, E., Collier, S., Horne, K., Filippenko, A. V., 1999, A&A, 341, 491–498.
27. Harlaftis, E. T. et al., 1999, MNRAS, 306, 348–352.
28. Harlaftis, E., 1999, A&A, 346, L73–L75.
29. Hastings, N. C. et al., 1999, PASP, 111, 177–183.
30. Heerlein, C., Horne, K., Schwöpe, A.D., 1999, MNRAS, 304, 145–154.
31. Hellier, C., Robinson, E.L., 1994, ApJL, 431, L107–L110.
32. Hellier, C., 1996, ApJ, 471, 949.
33. Hellier, C., 1997, MNRAS, 288, 817–832.
34. Hellier, C., 1999, ApJ, 519, 324–331.
35. Hessman, F.V., Hopp, U., 1990, A&A, 228, 387–398.
36. Hoard, D. W., Szkody, P., 1996, ApJ, 470, 1052.
37. Hoard, D. W., Szkody, P., 1997, ApJ, 481, 433.
38. Hoard, D. W. et al., 1998, MNRAS, 294, 689.
39. Horne, K., 1985, MNRAS, 213, 129–141.

40. Horne, K., 1991, Fundamental Properties of Cataclysmic Variable Stars: Proc. 12th North American Workshop on CVs and Low Mass X-Ray Binaries, ed. A. W. Shafter (San Diego: San Diego State Univ.), , 23–.
41. Howell, S. B., Ciardi, D. R., Dhillon, V. S., Skidmore, W., 2000, *ApJ*, 530, 904–915.
42. Joergens, V., Spruit, H. C., Rutten, R. G. M., 2000, *A&A*, 356, L33–L36.
43. Joergens, V. et al., 2000, *A&A*, 354, 579–588.
44. Kaitchuck, R. H. et al., 1994, *ApJS*, 93, 519–530.
45. Kaitchuck, R. H., Schlegel, E. M., White, J. C., Mansperger, C. S., 1998, *ApJ*, 499, 444.
46. Littlefair, S. P., Dhillon, V. S., Howell, S. B., Ciardi, D. R., 2000, *MNRAS*, 313, 117–128.
47. Marsh, T.R., 1985, PhD Thesis, Cambridge University.
48. Marsh, T.R., Horne, K., 1988, *MNRAS*, 235, 269–286.
49. Marsh, T. R. et al., 1990, *ApJ*, 364, 637–646.
50. Marsh, T.R., Horne, K., 1990, *ApJ*, 349, 593–607.
51. Marsh, T.R., Robinson, E.L., Wood, J.H., 1994, *MNRAS*, 266, 137.
52. Marsh, T.R., Duck, S.R., 1996, *New Astronomy*, 1, 97–119.
53. Marsh, T.R., 1999, *MNRAS*, 304, 443–450.
54. Martell, P. J., Horne, K., Price, C. M., Gomer, R. H., 1995, *ApJ*, 448, 380.
55. Mennickent, R. E., Diaz, M., 1996, *A&A*, 309, 147–154.
56. Mennickent, R. E., Diaz, M. P., Arenas, J., 1999, *A&A*, 352, 167–176.
57. Morales-Rueda, L., Marsh, T.R., Billington, I., 2000, *MNRAS*, 313, 454–460.
58. Nogami, D., Masuda, S., Kato, T., Hirata, R., 1999, *PASJ*, 51, 115–125.
59. North, R. C. et al., 2000, *MNRAS*, 313, 383–391.
60. Radon, J., 1917, *Ber. Verh. Sächs. Akad. Wiss. Leipzig Math. Phys. K1*, 69, 262–277.
61. Ratering, C., Bruch, A., Diaz, M., 1993, *A&A*, 268, 694–704.
62. Robinson, P.F.L., Marsh, T.R., Smak, J., 1999, *Accretion Disks in Compact Stellar Systems*, Edited by J. Craig Wheeler. World Scientific, ISBN 981-02-1273-9 (1993)., , 75–116.
63. Rowland, S.W., 1979, *Image Reconstruction from Projections*, , 8–79.
64. Rutten, R.G.M., Dhillon, V.S., 1994, *A&A*, 288, 773–781.
65. Schmidt, G. D. et al., 1999, *ApJ*, 525, 407–419.
66. Schwope, A.D., Mantel, K.-H., Horne, K., 1997, *A&A*, 319, 894–908.
67. Schwope, A. D. et al., 1998, *Wild stars in the old west: Proceedings of the 13th North American Workshop on Cataclysmic Variables and Related Objects*, eds. Howell, S. Kuulkers, E., Woodward, C., *astro-ph/9708228*, , 44–59.
68. Schwope, A. D. et al., 2000, *MNRAS*, 313, 533–546.
69. Shafter, A. W., Veal, J. M., Robinson, E. L., 1995, *ApJ*, 440, 853.
70. Shahbaz, T., Wood, J. H., 1996, *MNRAS*, 282, 362–372.
71. Simic, D. et al., 1998, *A&A*, 329, 115–130.
72. Smak, J., 1971, *Acta Astronomica*, 21, 15.
73. Smak, J., 1979, *Acta Astronomica*, 29, 309.
74. Smith, D.A., Dhillon, V.S., Marsh, T.R., 1998, *MNRAS*, 296, 465–482.
75. Spruit, H.C., Rutten, R.G.M., 1998, *MNRAS*, 299, 768–776.

- 76. Steeghs, D., Horne, K., Marsh, T.R., Donati, J.F., 1996, MNRAS, 281, 626–636.
- 77. Steeghs, D., Harlaftis, E.T., Horne, K., 1997, MNRAS, 290, L28–L32.
- 78. Still, M.D., Marsh, T.R., Dhillon, V.S., Horne, K., 1994, MNRAS, 267, 957.
- 79. Still, M. D., Dhillon, V. S., Jones, D. H. P., 1995, MNRAS, 273, 863–876.
- 80. Still, M. D., Dhillon, V. S., Jones, D. H. P., 1995, MNRAS, 273, 849–862.
- 81. Still, M. D., 1996, MNRAS, 282, 943–952.
- 82. Still, M. D., Buckley, D. A. H., Garlick, M. A., 1998, MNRAS, 299, 545–553.
- 83. Still, M.D., Duck, S.R., Marsh, T.R., 1998, MNRAS, 299, 759–767.
- 84. Still, M. D., Steeghs, D., Dhillon, V. S., Buckley, D. A. H., 1999, MNRAS, 310, 39–42.
- 85. Szkody, P., Armstrong, J., Fried, R., 2000, PASP, 112, 228–236.
- 86. Tovmassian, G. H. et al., 1997, A&A, 328, 571–578.
- 87. Tovmassian, G. H. et al., 1998, A&A, 335, 227–233.
- 88. Tovmassian, G. H. et al., 2000, ApJ, 537, 927–935.
- 89. Warner, B., Nather, R. E., 1971, MNRAS, 152, 219.
- 90. Welsh, W. F., Horne, K., Gomer, R., 1998, MNRAS, 298, 285–302.
- 91. White, J. C., Honeycutt, R. K., Horne, K., 1993, ApJ, 412, 278–287.
- 92. White, J. C., Schlegel, E. M., Honeycutt, R. K., 1996, ApJ, 456, 777.
- 93. Wolf, S. et al., 1998, A&A, 332, 984–998.
- 94. Wood, J. et al., 1986, MNRAS, 219, 629–655.

## Appendix A

In this appendix I show that, as stated in section 3.2, Eq. 5 can be inverted by application of the filter  $|s|/G(s)$  followed by the back-projection of Eq. 6. I define the Fourier transform  $F(s)$  of a function  $f(x)$ , and its inverse by

$$F(s) = \int_{-\infty}^{\infty} f(x) e^{-i2\pi s x} dx.$$

$$f(x) = \int_{-\infty}^{\infty} F(s) e^{i2\pi s x} ds.$$

The frequency  $s$  here is measured in cycles per unit  $x$ . Now take the Fourier transform over  $V$  of the line profile equation, 5:

$$F(s, \phi) = \int_{-\infty}^{\infty} f(V, \phi) e^{-i2\pi s V} dV \quad (9)$$

$$= \int_{-\infty}^{\infty} \int_{-\infty}^{\infty} I(V_x, V_y) \int_{-\infty}^{\infty} g(V - V_R) e^{-i2\pi s V} dV dV_x dV_y \quad (10)$$

$$= G(s) \int_{-\infty}^{\infty} \int_{-\infty}^{\infty} I(V_x, V_y) e^{-i2\pi s V_R} dV_x dV_y. \quad (11)$$

Dividing through by  $G(s)$ , multiplying by  $|s|$  and taking the inverse Fourier transform gives the filtered line profiles

$$\tilde{f}(V, \phi) = \int_{-\infty}^{\infty} \frac{|s| F(s, \phi)}{G(s)} e^{i2\pi s V} ds$$

$$= \int_{-\infty}^{\infty} \int_{-\infty}^{\infty} I(V_x, V_y) \int_{-\infty}^{\infty} |s| e^{-i2\pi s (V - V_R)} ds dV_x dV_y. \quad (12)$$

Finally, back-project these filtered profiles according to Eq. 6, that is compute the integral

$$\int_0^{0.5} \tilde{f}(V_R, \phi) d\phi,$$

where

$$V_R = \gamma - V_x \cos 2\pi\phi + V_y \sin 2\pi\phi. \quad (13)$$

Putting dashes on various symbols to avoid confusion later, then the back-projection integral becomes

$$\int_0^{0.5} \tilde{f}(V_R, \phi) d\phi = \int_{-\infty}^{\infty} \int_{-\infty}^{\infty} I(V'_x, V'_y) \int_0^{0.5} \int_{-\infty}^{\infty} |s| e^{-i2\pi s (V_R - V'_R)} ds d\phi dV'_x dV'_y$$

$$= \int_{-\infty}^{\infty} \int_{-\infty}^{\infty} I(V'_x, V'_y) \int_0^1 \int_0^{\infty} s e^{-i2\pi s (V_R - V'_R)} ds d\phi dV'_x dV'_y$$

$$= \int_{-\infty}^{\infty} \int_{-\infty}^{\infty} I(V'_x, V'_y) \delta(V'_x - V_x) \delta(V'_y - V_y) dV'_x dV'_y$$

$$= I(V_x, V_y). \quad (14)$$

The third line above follows from the second after transforming from polar coordinates  $s$  and  $\phi$  to cartesian  $s_x = s \cos 2\pi\phi$  and  $s_y = s \sin 2\pi\phi$ , and using Eqs. 13 so that

$$\int_0^1 \int_0^\infty s e^{-i2\pi s(V_R - V'_R)} ds d\phi = \int_{-\infty}^\infty \int_{-\infty}^\infty e^{-i2\pi[-(V_x - V'_x)s_x + (V_y - V'_y)s_y]} ds_x ds_y \quad (15)$$

and then the integrals over  $s_x$  and  $s_y$  separate to give the two Dirac  $\delta$ -functions of the penultimate line of Eq. 14 since

$$\delta(x) = \int_{-\infty}^\infty e^{\pm i2\pi s x} ds.$$

This justifies the assertions of section 3.2.



## Appendix B

**Table 2.** Doppler maps of CVs and X-ray novae published in refereed journals as of September 2000.

Object	Type	State	Res. km s <sup>-1</sup>	Line(s)	Features	Ref.
V616 Mon	BH	Q	80	H $\alpha$ , $\beta$	1; 2a; 3	51
GU Mus	BH	Q		H $\alpha$	3	9
V2107 Oph	BH	Q	120	H $\alpha$	1; 3	25
V518 Per	BH	O	100 (H $\beta$ ); 35 (H $\alpha$ )	H $\alpha$ , $\beta$ , HeII	1; 2?; 3	5
"	"	Q	120	H $\alpha$	1	26
QZ Vul	BH	Q	200	H $\alpha$	1; 2a	6
"	"	Q	120	H $\alpha$	1; 2a	24
AR And	DN	Q, O	180 (Q); 130 (O)	H $\alpha$ (Q); H $\beta$ , $\gamma$ (O)	1; 7	69
AE Aqr	DN	F	50	H $\alpha$	2b; 7	90
VY Aqr	DN	Q	300	P $\beta$	1?; 2b	46
OY Car	DN	O	80	H $\beta$	1; 2 or 4; 3	23
AT Cnc	DN	SS	140	H $\alpha$	2; 7	58
EM Cyg	DN	SS	35	H $\alpha$	1; 3	59
SS Cyg	DN	O	35	H $\alpha$ , $\beta$ , $\gamma$ , HeI, HeII	1; 3; 4?; 6	76
EX Dra	DN	?	80	H $\alpha$ , HeI, HeII	2ab; 3	2
"	DN	Q, O	100 – 250	H $\alpha$ – $\delta$ , HeI, CII	1; 2b	43
"	DN	O	35	H $\alpha$ , $\beta$ , HeI, HeII	1; 3; 4	42
U Gem	DN	Q	170	H $\beta$ , HeI, HeII	1; 2a; 3	49, 44
V2051 Oph	DN	Q	170	H $\beta$ , HeI	1; 7	44
IP Peg	DN	Q, O	150	H $\beta$ , $\gamma$ , HeII	1; 2ab; 3; 4	50
"	"	Q	170	H $\beta$	1; 7	44
"	"	Q	140	H $\alpha$	1; 3	22
"	"	O	35	H $\alpha$ , HeI	1; 3; 4; 6	76
"	"	O	35	H $\alpha$ , HeI	1; 3; 4	77
"	"	Q	70	H $\alpha$ , $\beta$ , $\gamma$	1; 2a, c; 3	93, 3
"	"	O	54	HeII, HeI, MgII	1; 3; 4; 6	27, 28
"	"	O	100	HeII, HeI, MgII, CII	1; 3; 4	57
KT Per	DN		200	H $\beta$	1	61
WZ Sge	DN	Q	170	H $\beta$ , HeI	1; 2a	44
"	DN	Q	90	H $\alpha$	1; 2a	75
"	DN	Q	300	P $\beta$	1; 2b	46
CU Vel	DN	Q	320	H $\alpha$	1	55

See end of Tab. 4 for notes.

**Table 3.** Doppler maps of CVs and X-ray novae published in refereed journals as of September 2000.

Object	Type	State	Res. km s <sup>-1</sup>	Line(s)	Features	Ref.
GD 552	DN?	Q	70	H $\beta$	1; 2	35
LY Hya	DN	Q	120	H $\beta$ , $\gamma$ , $\delta$	1; 2	78
GP Com	IBWD	—	70	HeI, HeII	1; 2; 6	53
FO Aqr	IP	—	80	HeII	2a; 3?	52
"	IP	—	80	HeII		34 <sup>†</sup>
BG CMi	IP	—	115	H $\beta$ , HeII	2	33, 34 <sup>†</sup>
PQ Gem	IP	—	115	H $\beta$ , HeII	2	33, 34 <sup>†</sup>
EX Hya	IP	—	170	H $\beta$	1; 2a	44
"	IP	—	65	H $\beta$		34 <sup>†</sup>
AO Psc	IP	—	80	HeII		34 <sup>†</sup>
V405 Aur	IP	—	50	H $\alpha$ , $\beta$ , HeI, HeII	1; 2b, d	83
"	"	—	120	H $\alpha$ , $\gamma$ , HeII	2b, d	85
RX0757+63	IP	—	280	H $\beta$	1; 2a	87
RX1238-38	IP	—	?	H $\beta$		34 <sup>†</sup>
RX1712-24	IP	—	?	HeII		34 <sup>†</sup>
DQ Her	N	—	170	H $\beta$ , HeI, HeII	1; 6	44
"	"	—	120	H $\gamma$ , HeI, HeII, CaII	1; 3	54
BT Mon	N	—	170	H $\beta$ , $\gamma$ , HeII	2b; 6; 7	44, 92
"	"	—	100, blue; 36, red	H $\alpha$ , $\beta$ , HeI, HeII	2b; 6	74
GQ Mus	N	—	220	HeII	1; 3	16
CP Pup	N	—	170	H $\beta$ , HeII	1	44, 91
PX And	NL	—	90	H $\alpha$	1; 2b	31
"	"	—	45	Balmer, HeII	2b, c; 7	79
V1315 Aql	NL	—	65	H $\beta$ , HeII	2b; 6; 7	11
"	"	—	170	H $\beta$ , HeI, HeII	2b; 6; 7	44
"	"	—	115	H $\beta$ , HeII	2b; 6; 7	32
UU Aqr	NL	—	170	H $\beta$	1; 2ab	44, 45
"	"	—	115	H $\alpha$ , $\beta$ , $\gamma$ , HeI, HeII	1; 2ab	38
V363 Aur	NL	—	170	H $\beta$ , HeII	2bc; 7	44
WX Cen	NL	—	130	H $\beta$ , HeII	1; 3; 7	18
AC Cnc	NL	—	170	H $\beta$ , HeII	2bd; 6; 7	44
V795 Her	NL	—	60	H $\beta$	1	20
"	"	—	70	H $\alpha$ , $\beta$ , $\gamma$ , HeI, HeII	1	7
BH Lyn	NL	L	75	H $\beta$ , $\gamma$ , $\delta$ , HeI	2b,c; 7	12
"	"	—	120	H $\beta$	1; 2c	37

For codes see Table 4.

<sup>†</sup>These maps were computed on the spin phase of the white dwarf rather than the standard orbital phase and thus I have not attempted to describe their features.

**Table 4.** Doppler maps of CVs and X-ray novae published in refereed journals as of September 2000.

Object	Type	State	Res. km s <sup>-1</sup>	Line(s)	Features	Ref.
BP Lyn	NL		120	H $\alpha,\beta,\gamma$	1; 2ad	36
"	"		80	H $\alpha$ , HeI	1; 2bc; 3	81
V347 Pup	NL	–	120	Balmer	1; 3; 4?	82
"	"	–	120	H $\beta$	2ab; 6	19
LX Ser	NL	–	170	H $\beta$ , HeI, HeII	2a, b; 6	44
SW Sex	NL	–	170	H $\beta$ , HeI	1; 2a; 6	44
"	"	–	75	H $\beta,\gamma,\delta$ , HeI, HeII	1; 2a; 6	14
VZ Scl	NL	–	170	H $\beta$	2ab; 7	44
RW Tri	NL	–	170	H $\beta$ , HeI, HeII	1, 3	44
"	"	H	50	H $\beta,\gamma$	3	80
DW UMa	NL	–	170	H $\beta$ , HeI, HeII	2b; 6	44
"	"	L	75	Balmer	3	13
UX UMa	NL	–	170	H $\beta$ , HeII	1; 6	44
HU Aqr	P	H	110	H $\gamma$ , HeII	3; 5	66, 30
AM Her	P	H	130	NV, SiIV, CIII (UV)	2b; 3; 7	21
V884 Her	P	H	200	H $\alpha,\beta$ , HeI, HeII	2ab	29
BL Hyi	P	H	160	H $\alpha$ , HeI	2a	56
ST LMi	P	–	70	NaI, CaII	3	70
"	"	L	350	NaI	3	41
V2301 Oph	P	H	80	H $\alpha,\beta,\gamma$ , HeI, HeII	3; 5?	71
VV Pup	P	H	90	H $\alpha$	3; 5	17
MR Ser	P	–	70	NaI, CaII	3	70
QQ Vul	P	H	70	NaI, MgII, HeII, Cl	3	10
"	"	H	100	HeII	3, 5	68
AR UMa	P	M	100	H $\alpha,\beta$ , HeI, HeII, MgI, NaI	3, 5	65
RX0719+65	P	H	300	H $\beta$ , HeII	2ab; 7	86
RX1015+09	P	H	?	HeII	3; 5	4
RX2157+08	P	H	180	H $\beta$ , HeII	3	88

Notes:

References are amalgamated when they refer to the same data.

Type codes: BH = black-hole system; DN = dwarf nova; N = old nova; NL = nova-like variable; IBWD = interacting binary white dwarf; IP = intermediate polar; P = polar. State codes (where relevant): Q = quiescence; O = outburst; SS = stand-still; F = flaring; H = high; L = low; M = middle.

Feature codes: (1) Ring (which may be from a disc), (2) Spot, (3) Secondary star, (4) Spiral shocks, (5) Gas stream, (6) Low velocity emission, (7) Little structure or low signal-to-noise.

Type (2) = “spot” does not necessarily imply stream/disc impact, but just refers to the appearance of the image. Entries such as 2a refer to the quadrant the spot is located in (if the orbital phase is known). The quadrants start at the upper-left with “a”, and then go anti-clockwise from there. A combination such as 2ab implies a spot located on the boundary of the upper-left and lower-left quadrants.

Type (6) = “low-velocity emission” refers to such features as the slingshot prominences seen in IP Peg [76] and the emission at low velocities commonly seen in nova-like variables.